

# Journal of Materials Chemistry A

Materials for energy and sustainability

Accepted Manuscript

This article can be cited before page numbers have been issued, to do this please use: K. Huang, S. AlSobhi, Z. Shen, Z. Li, N. G. West, S. J. Skinner, A. Walton, G. Wilson and J. Xu, *J. Mater. Chem. A*, 2026, DOI: 10.1039/D6TA03119F.



This is an Accepted Manuscript, which has been through the Royal Society of Chemistry peer review process and has been accepted for publication.

Accepted Manuscripts are published online shortly after acceptance, before technical editing, formatting and proof reading. Using this free service, authors can make their results available to the community, in citable form, before we publish the edited article. We will replace this Accepted Manuscript with the edited and formatted Advance Article as soon as it is available.

You can find more information about Accepted Manuscripts in the [Information for Authors](#).

Please note that technical editing may introduce minor changes to the text and/or graphics, which may alter content. The journal's standard [Terms & Conditions](#) and the [Ethical guidelines](#) still apply. In no event shall the Royal Society of Chemistry be held responsible for any errors or omissions in this Accepted Manuscript or any consequences arising from the use of any information it contains.

# Ammonia decomposition on $\text{LaV}(\text{O},\text{N})_{3-\delta}$ surfaces: toward a mechanistic understanding

View Article Online  
DOI: 10.1039/C6TA03119F

Kehan Huang,<sup>a†</sup> Samia Al Sobhi,<sup>b†</sup> Zonghao Shen,<sup>a</sup> Zhenzhu Li,<sup>a</sup> Alex S. Walton,<sup>c</sup> Norton West,<sup>c</sup> George Wilson,<sup>b</sup> Jingdong Xu,<sup>b</sup> and Stephen J. Skinner<sup>a, b, d\*</sup>

<sup>a</sup> Imperial Global Singapore (IGS), 1 CREATE Way, #11-01, CREATE Tower, Singapore 138602, Singapore.

<sup>b</sup> Department of Materials, Imperial College London, South Kensington, London SW7 2AZ, UK.

<sup>c</sup> Department of Chemistry and Photon Science Institute, The University of Manchester, Manchester M13 9PL, UK.

<sup>d</sup> International Institute for Carbon Neutral Energy Research, Kyushu University, Fukuoka 819-0395, Japan.

† The authors contributed equally to this work.

\* The corresponding author

## ABSTRACT

Ammonia, as a carbon-free hydrogen carrier, provides an efficient pathway for hydrogen transport, storage and utilisation in the green energy transition. To recover hydrogen from ammonia, perovskite-structured oxynitrides show promise as noble metal-free catalysts for ammonia decomposition, offering both encouraging catalytic performance and highly tuneable electronic properties. However, understanding of the critical catalytic pathways of these materials remains unresolved, with the nature of the active sites for ammonia decomposition on perovskite oxynitrides unclear. In this work,  $\text{LaV}(\text{O},\text{N})_{3-\delta}$  oxynitrides with varying nitrogen contents were synthesised and found to exhibit good catalytic activity. Machine learning interatomic potential (MLIP) simulations were employed to investigate the underlying mechanisms, revealing that anion vacancies play a critical role as active sites for ammonia decomposition. Furthermore, near-ambient pressure X-ray photoelectron spectroscopy (NAP-XPS) measurements were performed, showing the continuous surface nitridation processes occurring on the  $\text{LaV}(\text{O},\text{N})_{3-\delta}$  oxynitride. These results provide new insights into the reaction mechanisms of ammonia decomposition and underscore the innovative



potential of perovskite oxynitrides as a pioneering class of noble metal-free catalysts paving the way for sustainable hydrogen production through efficient ammonia decomposition.

View Article Online  
DOI: 10.1039/D6TA03119F



## 1. Introduction

Ammonia ( $\text{NH}_3$ ) is among the highest-volume industrial chemicals, widely used as a fertiliser, refrigerant, and as a precursor to numerous chemical products.<sup>1</sup> Over recent years, ammonia has attracted significant attention as a zero-carbon hydrogen carrier due to its high liquefied volumetric hydrogen content and its well-established infrastructure for storage and transportation compared to hydrogen itself.<sup>1–3</sup> To recover hydrogen ( $\text{H}_2$ ) from the energy carrier,  $\text{NH}_3$ , the development of efficient catalytic ammonia decomposition (cracking) is of significant importance.<sup>4,5</sup> Meanwhile, the direct use of ammonia as a fuel, particularly in direct ammonia solid oxide fuel cells (DA-SOFCs)<sup>6–8</sup> that enable the direct conversion of ammonia into electricity, represents another potential research direction.

To catalytically crack or decompose ammonia with energy efficiency and low-cost, highly effective catalysts with long durability play a central role. Among the reported catalysts in the open literature, ruthenium (Ru)-based catalysts present superior activity compared to other transition metal (Fe, Ni, Co)-based mono- or bi-metallic catalysts.<sup>4,9–11</sup> For example, a high conversion rate of over 80% has been maintained at 550 °C up to 40 bar using potassium promoted Ru on a CaO support,<sup>12</sup> while others such as supported Ni catalysts normally require much higher temperatures with potential risks of nitridation further degrading catalyst performance.<sup>13</sup> However, the inherently high cost of Ru hinders its broader utilisation and research on alternative catalytical systems remain of great research significance.

Of particular interest, inorganic metal nitrides<sup>14–16</sup> and oxynitrides<sup>17,18</sup> have demonstrated their potential for catalysing ammonia decomposition, with their high resistance to harsh ammonia conditions at elevated temperatures. In addition, it has been reported that anion vacancy sites play important roles in mediating ammonia decomposition.<sup>18,19</sup> Density functional theory (DFT) has revealed that for the  $\text{Ni-BaTiO}_{3-x}\text{N}_y$  system instead of the Ni surface,  $\text{NH}_3$  is preferentially adsorbed on the anion vacancies of the oxynitride surfaces<sup>19</sup>, highlighting the significant importance of anion vacant sites in these nitride and oxynitride phases for ammonia decomposition. Oxynitrides or more broadly speaking mixed-anionic compounds, particularly perovskite-structured oxynitride materials with a high tolerance of foreign cations,



anions and vacancies, provide ideal platforms for tuning material chemistries and structures, as well as their optical, (thermo-, di-) electrical and magnetic properties.<sup>20–</sup>

<sup>22</sup> For example, remarkably high bulk dielectric constants have been reported for Ta-based oxynitride ATaO<sub>2</sub>N (A= Sr, Ba)<sup>23</sup> and notably small optical band gaps have been reported for phases such as LaNbON<sub>2</sub> (1.7 eV)<sup>24</sup> and CeNbO<sub>1.5</sub>N<sub>1.5</sub> (1.8 eV)<sup>25</sup>, compared with their oxide precursors. In addition, anion arrangements (ordered, partially ordered or completely disordered) in the coordination octahedra, which are still difficult to manipulate, are suggested to have further impacts on material properties.<sup>25–27</sup> Different sample preparation routes have been proposed as a possible reason for the anion arrangements in some oxynitrides, such as SrMO<sub>2</sub>N (M=Ta, Nb)<sup>28,29</sup> while being irrelevant for others, such as LaTiO<sub>2</sub>N.<sup>30</sup> Despite the promising and intriguing performance of the metal oxynitride phases, they remain largely untapped compared with their oxide parents.

In terms of the catalytic performance of the oxynitrides, studies are mainly performed in the photocatalytic directions such as visible-light-driven water splitting<sup>31</sup> and organic pollutant decomposition,<sup>32</sup> since the N 2*p* band lies above the O 2*p* band resulting in a reduced band gap after N incorporation into the metal oxide lattice. However, although several encouraging preliminary studies on oxynitrides exist, the potential of perovskite-structured oxynitrides for ammonia decomposition or application as anode materials in DA-SOFCs remains to be explored, particularly with advanced *in situ* characterisation tools to explore the reaction mechanisms.

In this work, LaV(O,N)<sub>3-δ</sub> powders with a multivalent transition metal (vanadium, V<sup>x+</sup>) on the B-site, thus with both tuneable anionic ratio and anion vacancies, have been prepared. Two different synthesis methods were applied to prepare their oxide precursors with different surface areas and morphologies. Their catalytic performance towards ammonia decomposition was further investigated and compared with that of a fully ordered, stoichiometric LaTaON<sub>2</sub> phase with a *d*<sup>0</sup> B-site cation (tantalum, Ta<sup>5+</sup>). Machine learning interatomic potential (MLIP) simulations were conducted, indicating the critical role of anion vacancies as catalytically active sites for ammonia decomposition. Furthermore, near-ambient pressure X-ray photoelectron spectroscopy (NAP-XPS) was carried out at elevated temperatures under ammonia to observe ammonia adsorption at the surface and phase nitridation.



## 2. Experimental

### 2.1 Sample preparation

LaV(O,N)<sub>3-5</sub> and LaTaON<sub>2</sub> oxynitride powders were prepared by nitridation of their corresponding oxide precursors under flowing ammonia at elevated temperature. Two LaVO<sub>4</sub> precursors were synthesised via the solid-state reaction and coprecipitation methods respectively. The LaTaO<sub>4</sub> oxide precursor was obtained via the standard polymerised-complex (PC) method.<sup>33</sup>

#### 2.1.1 Solid state reaction

Prior to weighing, La<sub>2</sub>O<sub>3</sub> (Alfa Aesar, 99.99%) was preheated at 900 °C for 12 hrs to ensure full dehydration. Stoichiometric amounts of La<sub>2</sub>O<sub>3</sub> and V<sub>2</sub>O<sub>5</sub> (Alfa Aesar, 99.6%) were thoroughly mixed and ground manually in an agate mortar using anhydrous ethanol as a suspension medium. The mixture was calcined in air at 1000 °C for 12 h, reground, and further calcined at 1200 °C for 12 hrs. Phase purity of the resulting LaVO<sub>4</sub> was confirmed by X-ray diffraction (XRD). The LaVO<sub>4</sub> powder was then annealed at 800 °C for 6 hrs under a flow of pure NH<sub>3</sub> (BOC, 99.98%) at 100 cm<sup>3</sup>·min<sup>-1</sup>. Subsequently, the sample was cooled to 100 °C under NH<sub>3</sub> flow and then purged with Ar (BOC, 99.998%). The resulting black powder was ground to a fine powder and labelled as **LaVON-S**.

#### 2.1.2 Coprecipitation method

1 mmol of ammonium metavanadate (NH<sub>4</sub>VO<sub>3</sub>) was dissolved in 100 mL of deionised water and acidified to pH=3 using 50% dilute nitric acid. Subsequently, 1 mmol of lanthanum (III) nitrate hexahydrate (La(NO<sub>3</sub>)<sub>3</sub>·6H<sub>2</sub>O, Sigma-Aldrich, 99.9%) was added. The mixture was heated at 70 °C under constant stirring, and aqueous ammonia (NH<sub>3</sub>·H<sub>2</sub>O) was added dropwise until a yellow precipitate formed at pH=7. The precipitate was filtered, washed off repeatedly with deionised water and ethanol, dried at 60 °C overnight, and finally calcined in air at 600 °C for 6 hrs. The obtained LaVO<sub>4</sub> precursor was then subjected to the same thermal ammonolysis as described above for LaVON-S, and the final product was labelled as **LaVON-P**.



### 2.1.3 Synthesis of LaTaON<sub>2</sub>

View Article Online  
DOI: 10.1039/D6TA03119F

In a typical PC procedure, 3.1 mmol tantalum pentachloride (TaCl<sub>5</sub>, Sigma-Aldrich, 99.9%) and anhydrous citric acid were dissolved in 10 mL ethylene glycol. Subsequently, 3.10 mmol lanthanum nitrate hexahydrate (La(NO<sub>3</sub>)<sub>3</sub>·6H<sub>2</sub>O, Sigma-Aldrich, 99.9%) was added to the solution. The mixture was then heated at 200 °C and stirred for 2 hrs until a transparent gel formed. Upon further heating to 300 °C for 3 hrs to promote polymerisation, the gel changed colour from transparent to brown. The resulting resin was calcined in air at 550 °C for 10 hrs to remove the organic species. Ammonolysis was then carried out by annealing the obtained white amorphous oxide powder in a tube furnace under NH<sub>3</sub> gas flow (240 cm<sup>3</sup>·min<sup>-1</sup>, BOC, 99.98%) at 1050 °C for 10 hrs, after which the product was ground into black powders.

### 2.2 Material characterisation

Phase purity was assessed using a Bruker D2 Phaser diffractometer with Cu K<sub>α</sub> radiation ( $\lambda = 1.5418 \text{ \AA}$ ). Data were collected over a  $2\theta$  range of 20-80° with a step size of 0.02°. Rietveld refinements were performed using the GSAS-II software with a reference structure of LaVO<sub>2.78</sub>N<sub>0.10</sub> (ICSD: 247952).<sup>34,35</sup>

High-resolution transmission electron microscopy (HRTEM) images were acquired on a JEOL JEM-2100F microscope operated at 300 kV. Samples were prepared by sonicating the powder in high-purity isopropanol and drop-casting the dispersion onto holey carbon-coated Cu grids (3.05 mm diameter, 300 mesh, TAAB). The *d*-spacing value was determined using ImageJ software.

Specific surface areas were determined by the Brunauer-Emmett-Teller (BET) method from N<sub>2</sub> adsorption-desorption isotherms measured at 77 K using a Micromeritics Tristar II instrument (Malvern Panalytical Ltd., UK). Prior to each measurement, samples were degassed overnight at 120 °C under vacuum.

Carbon, hydrogen, and nitrogen (CHN) contents were quantified by dynamic flash combustion analysis using a FlashEA 1112 Series CHNS-O Analyser (Thermo Fisher Scientific, UK). The measurements were outsourced to Medac Ltd. (UK). During analysis, the combustion gases were mixed with a helium carrier gas and



subsequently swept to a chromatographic separation column, where they were detected using a thermal conductivity detector (TCD). View Article Online  
DOI: 10.1039/D0TA03119F

Conventional X-ray photoelectron spectroscopy (XPS) measurements were performed using a K-Alpha spectrometer (Thermo Fisher Scientific Ltd., UK) with a monochromatic Al  $K_{\alpha}$  radiation source ( $h\nu = 1486.6$  eV) and a spot size of 400  $\mu\text{m}$  at a base pressure below  $8 \times 10^{-8}$  mbar. The near-ambient pressure X-ray photoelectron spectroscopy (NAP-XPS) experiments were carried out using a SPECS NAP-XPS system with monochromatic Al  $K_{\alpha}$  radiation ( $h\nu = 1486.6$  eV, at 25 W) and a spot size of 300  $\mu\text{m}$ . Emitted photoelectrons were detected using a SPECS Phoibos 150 NAP differentially pumped analyser. The sample was first degassed under ultra-high vacuum (UHV,  $< 5 \times 10^{-9}$  mbar) at room temperature. Then, the NAP cell was conditioned to the desired temperature (thermocouple readings within  $\pm 10$  K) and  $3 \pm 0.05$  mbar  $\text{NH}_3$ . The correlated residual gas mass spectrometry signals (MKS e-vision 2) of  $\text{NH}_3$ ,  $\text{N}_2$ , and  $\text{H}_2$  to confirm catalyst activity during NAP-XPS measurements. The system was held at equilibrium for  $> 60$  min before data acquisition. All binding energies were calibrated to C 1s peak at 284.8 eV. Spectral deconvolution was performed using Avantage software (Thermo Fisher Scientific Inc., UK).

### 2.3 Machine learning interatomic potential simulation

The computational studies based on machine learning interatomic potential (MLIP) simulation were performed using the Many-body Atomic Cluster Expansion (MACE) package with the foundation model **mace-mh-1**.<sup>36,37</sup> Given the complexity of the  $\text{LaV}(\text{O},\text{N})_{3-\delta}$  supercell, 20 supercells with LaO/N surface termination and different possible defect configurations were randomly generated. Structural relaxations were performed using the BFGS structural optimisation algorithm within the Atomic Simulation Environment (ASE) package, with a force convergence criterion of 0.001 eV/Å.<sup>38,39</sup> The supercell with the lowest energy after structural relaxation was chosen for the follow-up computational studies. Meanwhile, hypothetical  $\text{LaVO}_3$  and  $\text{LaVON}_2$  supercells with LaO/N surface termination were configured and relaxed for the direct comparison.



## 2.4 Catalytic tests for ammonia decomposition

View Article Online  
DOI: 10.1039/D6TA03119F

The catalytic performance for ammonia decomposition was evaluated in a fixed-bed reactor at ambient pressure (schematic in Figure S1 of the supplementary information). 0.1 g sample powders were loaded between alumina wool plugs in an alumina tube reactor. Prior to reaction, the catalyst was activated at 500 °C for 1 hr under Ar at a flow rate of 50 cm<sup>3</sup>·min<sup>-1</sup>, then cooled to 250 °C. The feed gas was switched to 5% NH<sub>3</sub>/Ar (BOC, NH<sub>3</sub> anhydrous 99.98%; Ar 99.998%) at a flow rate of 5 cm<sup>3</sup>·min<sup>-1</sup>. Reactions were conducted at temperature ranging from 450-600 °C, with a step of 50 °C. Upon reaching each temperature, samples were held for 30 min to ensure equilibrium conditions. All the gas lines were maintained at 70 °C to prevent NH<sub>3</sub> condensation and subsequent corrosion. To eliminate the residual hazardous ammonia gas, the outlet gas was treated through ice baths and further analysed by a CatalySys quadrupole mass spectrometer system (ESS Ltd., UK). Prior to the sample measurements, baseline signals were recorded using the feed gas at different flow rates for calibration. The system was purged with Ar before NH<sub>3</sub> introduction and after reaction completion. The ammonia conversion rate, NH<sub>3 conv.</sub>, was calculated accordingly as:

$$\text{NH}_3 \text{ conv.} = \frac{(\text{NH}_3 \text{ inlet} - \text{NH}_3 \text{ outlet})}{\text{NH}_3 \text{ inlet}}$$

## 3. Results and discussion

### 3.1 Structure and composition

Figure 1 presents the XRD patterns of the two LaV(O,N)<sub>3-δ</sub> samples prepared using different synthesis methods, showing a single-phase nature within the detection limit of laboratory X-ray diffraction instrumentation. Both samples crystallise in a perovskite-type orthorhombic crystal structure (space group *Pnma*) that align well with previous reports.<sup>34</sup> Meanwhile, as shown in the magnified view of Figure 1(a), the peaks of LaVON-P shift slightly toward lower  $2\theta$  angles, indicating a larger lattice in LaVON-P compared to LaVON-S.



Table 1 Rietveld refinement results of LaVON-S and LaVON-P, respectively. View Article Online  
DOI: 10.1039/D6TA03119F

	LaVON-S	LaVON-P
a (Å)	5.5514(7)	5.5527(9)
b (Å)	7.8628(8)	7.8670(8)
c (Å)	5.5466(8)	5.5492(9)
V (Å <sup>3</sup> )	242.104(8)	242.409(12)
$\chi^2$	1.34	1.24

Figure S2(a) and (b) of the supplementary information present the Rietveld refinement data of LaVON-S and LaVON-P, respectively, and the key parameters derived from these refinements are summarised in Table 1. Refining the O/N ratio using XRD is challenging due to the dominant contribution from the heavier cations and the nearly identical X-ray atomic scattering factors of oxygen and nitrogen.<sup>29,34</sup> Figure 1(b) and (c) present HRTEM images of LaVON-S and LaVON-P samples, showing clear lattice fringes, which indicates a high degree of crystallinity for both samples.

Nitridation and the surface chemistry of LaVON-S were further evaluated using XPS. Figure 2(a)-(d) displays XPS spectra of La 3d, V 2p<sub>3/2</sub>, O 1s, and N 1s, respectively. The well-defined multiplet-split peaks with the plasmon loss feature indicate the oxidation state of La<sup>3+</sup>. The energy splitting of 4.2 eV in La 3d<sub>5/2</sub> serves as an indicator of the chemical state of the La<sup>3+</sup> cations, suggesting its anhydrous oxide nature.<sup>40</sup> A close inspection of the XPS spectrum of V 2p<sub>3/2</sub> reveals the presence of multiple oxidation states from V<sup>5+</sup> to V<sup>x+</sup> (0 < x < 3), where the unambiguous assignment of V<sup>x+</sup> remains challenging.<sup>41,42</sup> The atomic ratio of these V cations was V<sup>5+</sup>: V<sup>4+</sup>: V<sup>3+</sup>: V<sup>x+</sup> = 60.0%: 22.2%: 13.5%: 4.3%. Meanwhile, the atomic ratio of La and V cations was 51.6%: 48.4%, within experimental error, which is close to the theoretical ratio.



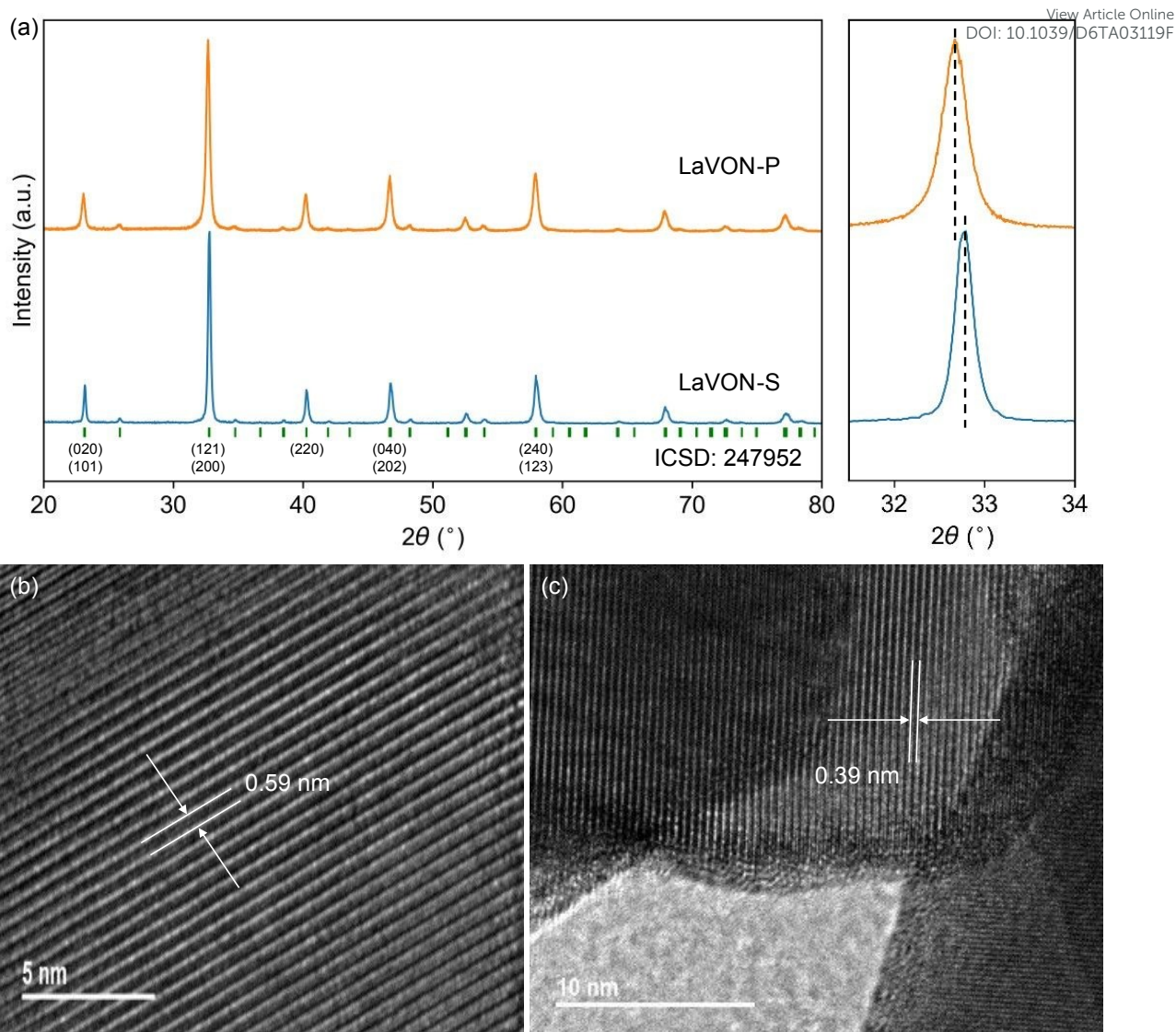


Figure 1 (a) XRD patterns of LaVON-S and LaVON-P powders, respectively. A subfigure on the right shows a magnified view of the  $2\theta$  range of  $31^{\circ}$ – $34^{\circ}$ , indicating the peak shift; HRTEM images of (b) LaVON-S and (c) LaVON-P, respectively. The  $d$ -spacings of the well-crystallised lattice fringes were estimated to be 0.59 nm and 0.39 nm, respectively.

With regard to anions, the O 1s XPS spectrum presents distinct oxygen species that can be assigned as lattice oxygen (M-O), surface-adsorbed hydroxy groups (O-H) and carbon containing species (O-C=O), respectively, while the N 1s XPS spectrum clearly shows a nitride peak (M-N), confirming nitridation.<sup>43,44</sup> It is worth mentioning that some peaks in the V  $2p_{3/2}$  spectrum could also be assigned to VN species. However, given that the amount of N obtained from the XPS fitting was small, where the atomic ratio between O and N was approximately 95.2%: 4.8%, the contribution from VN is thus considered to be negligible.



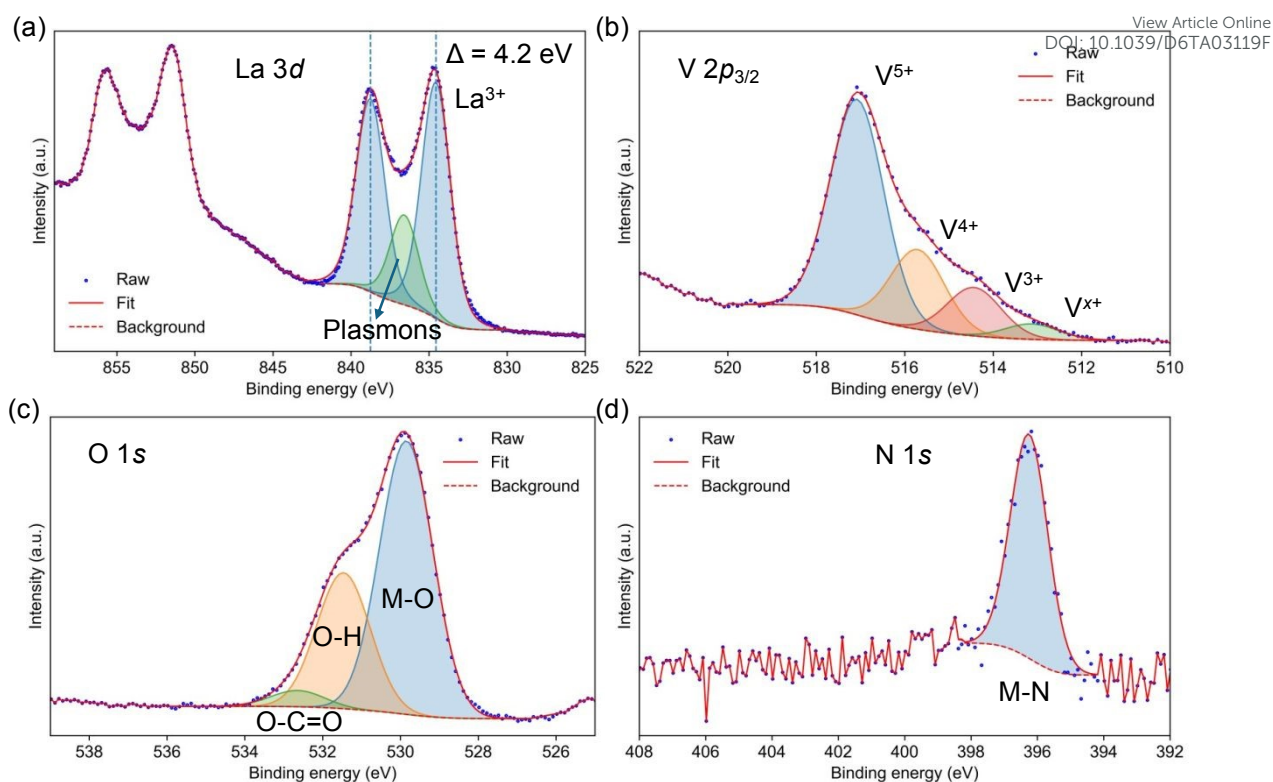


Figure 2 XPS spectra of (a) La 3d, (b) V 2p<sub>3/2</sub>, (c) O 1s, and (d) N 1s in LaVON-S, respectively. V<sup>x+</sup> in (b) represents the V cations with lower oxidation states (0 < x < 3).

### 3.2 Catalytic tests for ammonia decomposition

The catalytic activities of both LaVON-S and LaVON-P powders for ammonia decomposition were explored at elevated temperatures under 5% NH<sub>3</sub>/Ar. Prior to the catalytic performance measurements, and in order to further understand and interpret the effects of surface area and nitrogen content on catalytic activity, BET surface area measurements and CHN elemental analysis were performed on both LaVON samples, and the data are summarised in Table 2. A large surface area of 42 m<sup>2</sup>·g<sup>-1</sup> was obtained for LaVON-P, whereas that of LaVON-S was below 5 m<sup>2</sup>·g<sup>-1</sup>, indicating a pronounced influence of the preparation method on the surface area. The low surface area on LaVON-S is likely attributable to high-temperature annealing, which promotes particle growth. In addition, the nitrogen content in LaVON-S was approximately twice than of the LaVON-P. However, both values were very low overall, likely due to the short ammonia annealing time and relatively low ammonolysis temperature, which is consistent with the XPS fitting results and the literature.<sup>34</sup> In addition, the reported chemical composition was estimated under the assumption of a stoichiometric anion sublattice (O+N=3); however, in practice, anion vacancies are expected with multivalent V<sup>x+</sup> and after N-incorporation.



Table 2 BET surface area and N content from CHN elemental analysis of LaVON-S, LaVON-P and LaTaON<sub>2</sub>, respectively. The chemical formula was established from N content by assuming O+N=3.

	Surface area (m <sup>2</sup> ·g <sup>-1</sup> )	N content (wt%)	Chemical formula
LaVON-S	<5	1.02	LaVO <sub>2.83</sub> N <sub>0.17</sub>
LaVON-P	42	0.59	LaVO <sub>2.90</sub> N <sub>0.10</sub>
LaTaON <sub>2</sub>	<5	7.00	LaTaO <sub>1.18</sub> N <sub>1.82</sub>

To better distinguish the effect of surface area and anion vacancies introduced by nitridation, a state-of-the-art stoichiometric oxynitride system with *d*<sup>0</sup> transition metal and more ordered O/N arrangement, LaTaON<sub>2</sub>, was prepared as a reference material with a low surface area and a significantly higher nitrogen content.<sup>45,46</sup> Despite its high nitrogen content, the concentration of anion vacancies in LaTaON<sub>2</sub> is low due to its stoichiometric composition.<sup>45,46</sup>

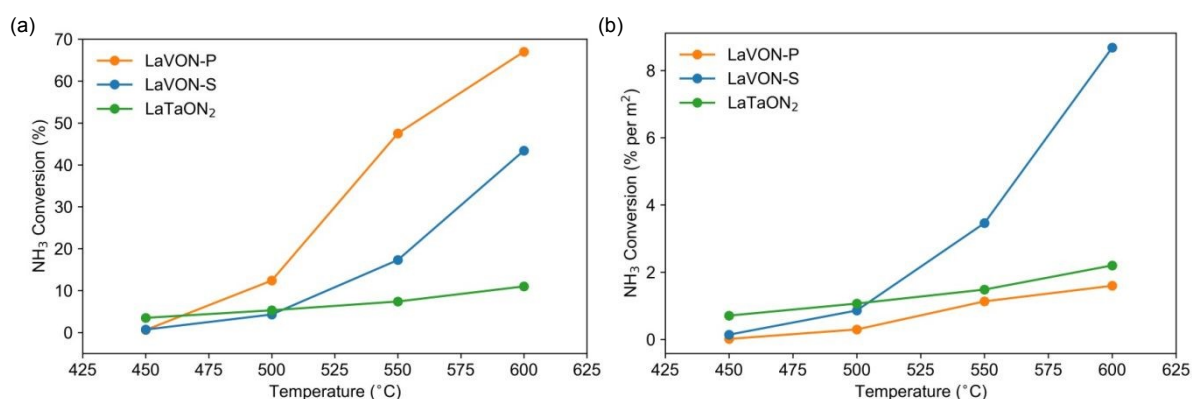


Figure 3 (a) Catalytic activity and (b) surface area specific catalytic activity of LaVON-S, LaVON-P, and LaTaON<sub>2</sub> for NH<sub>3</sub> decomposition reaction in the temperature range of 450-600 °C, respectively. The surface area specific catalytic activity of LaVON-S and LaTaON<sub>2</sub> were obtained by assuming their surface area was 5 m<sup>2</sup>·g<sup>-1</sup>.

Figure 3(a) presents the effective ammonia decomposition activities of LaVON-S, LaVON-P, and LaTaON<sub>2</sub> catalysts, respectively. The corresponding ammonia conversion and hydrogen production results are summarised in Table 3. Note that the hydrogen production rate among each sample is not directly comparable due to the different baseline calibrations. The performance of all three samples increased significantly with rising temperature, owing to the endothermic nature of the reaction.<sup>47,48</sup> In contrast, LaTaON<sub>2</sub> exhibited very low catalytic activity, which increased only marginally with increasing temperature. LaVON-P exhibited the highest catalytic activity among LaVON-P, LaVON-S and LaTaON<sub>2</sub>, primarily due to its larger surface area. The apparent activation energy for LaVON-P was 70.3 kJ/mol, which is comparable to that of the highly active catalyst Co<sub>3</sub>Mo<sub>3</sub>N (70.3 kJ/mol) for ammonia decomposition.<sup>49</sup> However, surface area can have a crucial effect on the catalytic activity. To mitigate its effect, the NH<sub>3</sub> conversion rates of the three catalysts are



normalised by surface area as shown in Figure 3(b). A lower bound of reliable values (5 m<sup>2</sup> g<sup>-1</sup>) is used for the surface area of both LaVON-S and LaTaON<sub>2</sub> due to inherent limitations of the BET measurements. After normalisation, interestingly, LaVON-S demonstrated the highest surface-area-specific ammonia conversion rate, while the conversion rate of LaTaON<sub>2</sub> remained very low. The high catalytic performance of the LaVON-S sample is likely related to its under-stoichiometric anionic sublattice. It has been proposed that anion vacancies introduced by nitridation are potential catalytically active sites in oxynitrides.<sup>17–19</sup> Compared to the stoichiometric LaTaON<sub>2</sub> sample and the LaVON-P with lower N incorporation, LaVON-S presents higher anion vacancy concentration, highlighting the crucial role of anion vacancies in ammonia decomposition.<sup>17,50</sup> To be noted, in the case that the actual surface area is smaller than the assumed value of 5 m<sup>2</sup>·g<sup>-1</sup>, the surface-area-specific catalytic activity of LaVON-S would be even higher, which further highlights the effect of anion vacancies. Furthermore, it is important to note that the catalytic activity tests were conducted using 5%NH<sub>3</sub>/Ar. Ammonia conversion under pure NH<sub>3</sub> is expected to be higher.<sup>51</sup>

Table 3 Ammonia conversion rate and hydrogen production rate of LaVON-S, LaVON-P and LaTaON<sub>2</sub> catalysts, respectively.

Temperature (°C)	LaVON-S		LaVON-P		LaTaON <sub>2</sub>	
	Ammonia conversion rate (%)	Hydrogen production rate (μmol·h <sup>-1</sup> ·g <sup>-1</sup> )	Ammonia conversion rate (%)	Hydrogen production rate (μmol·h <sup>-1</sup> ·g <sup>-1</sup> )	Ammonia conversion rate (%)	Hydrogen production rate (μmol·h <sup>-1</sup> ·g <sup>-1</sup> )
450	0.7	0.29	0.6	0.35	3.5	0.61
500	4.3	0.49	12.4	0.54	5.3	0.65
550	17.3	1.57	47.5	1.96	7.5	0.68
600	43.4	4.76	67.0	7.03	11.0	0.93

### 3.3 Machine learning interatomic potential (MLIP) simulations

MLIP simulations were performed to investigate the critical role of anion vacancies and ammonia decomposition on the catalyst surfaces. Ammonia molecules were initially placed at random positions within the vacuum layer above the surface, at varying heights. As shown in Figure 4(a), after multiple structural relaxations, NH<sub>3</sub> was consistently found to adsorb preferentially at the top site, with adsorption energies of approximately -0.9 eV across all surface configurations. Following adsorption, NH<sub>3</sub><sup>\*</sup> readily dissociates to release one hydrogen atom, and the resulting NH<sub>2</sub><sup>\*</sup> species



migrates to the bridge site on all surfaces. This intermediate is stabilised by nearby nitrogen anions and, more effectively, by anion vacancies.

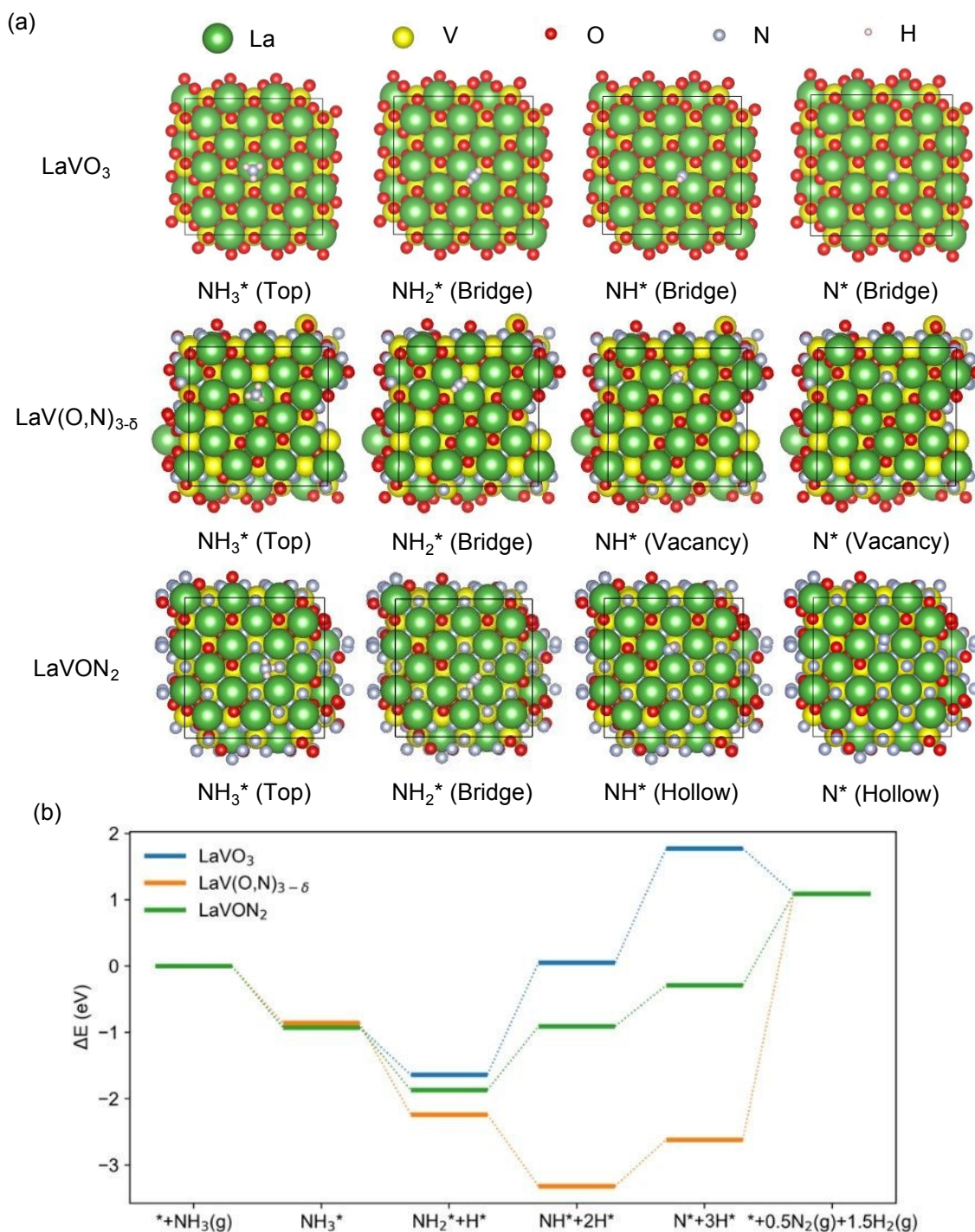


Figure 4 (a) The stable adsorption site for the chemical species involved in ammonia decomposition on different surfaces. (b) Energy profile along the reaction path for ammonia decomposition on different surfaces. The reference energy ( $\Delta E = 0$  eV) refers to an isolated  $\text{NH}_3$  molecule and naked surfaces. The numerical data of all the reaction steps are summarized in Table S1.

In contrast, the subsequent intermediates  $\text{NH}^*$  and  $\text{N}^*$  exhibit distinct adsorption behaviours depending on the surface composition. As illustrated in Figure 4(b) and Table S1, on the  $\text{LaVO}_3$  surface, both  $\text{NH}^*$  and  $\text{N}^*$  remain at bridge sites likely due to



Coulombic repulsion between the adsorbates and oxygen anions, resulting in highly unfavourable (less negative) adsorption energies. These weak interactions correlate with the poor calculated catalytic activity for  $\text{LaVO}_3$ .

Substituting oxygen with nitrogen in  $\text{LaVON}_2$  enables  $\text{NH}^*$  and  $\text{N}^*$  to occupy hollow sites adjacent to nitrogen anions, which lowers their adsorption energies by roughly half compared to  $\text{LaVO}_3$ . This energetic improvement aligns with the modest catalytic activity seen in stoichiometric oxynitrides discussed earlier. Meanwhile, in the defective oxynitride  $\text{LaV(O,N)}_{3-\delta}$ , anion vacancies create stable adsorption sites for both  $\text{NH}^*$  and  $\text{N}^*$ , significantly promoting the decomposition steps. However, the strong binding at these vacancies may hinder the desorption of final products, potentially limiting turnover.

In summary, these computational results effectively demonstrate that anion vacancies are essential for facilitating ammonia adsorption and enabling efficient decomposition, highlighting their role as key catalytically active sites in perovskite oxynitrides. It should be noted that the endothermic nature of ammonia decomposition corresponds to a net energy change of +0.42 eV. However, this value is not fully captured in the present calculations due to the absence of free energy corrections (e.g., zero-point energy, entropic contributions, and temperature effects). Nevertheless, the observed trends in adsorption energies and reaction pathways are consistent with the experimental findings and previous studies.<sup>17,19</sup>

### 3.4 NAP-XPS study under ammonia

To further understand ammonia decomposition on the surface of  $\text{LaV(O,N)}_{3-\delta}$ , NAP-XPS measurements were performed with four successive steps: (S1) at 250 °C under UHV, (S2) at 240 °C under 3 mbar  $\text{NH}_3$ , (S3) at 546 °C under 3 mbar  $\text{NH}_3$ , and (S4) at 250 °C under UHV. Figure 5(a)-(d) present the NAP-XPS spectra of La 3d, V 2p together with O 1s, N 1s, and valence band maximum (VBM) for  $\text{LaVON-P}$ . For La 3d spectra, consistent with Figure 3(a), the energy splitting in La 3d<sub>5/2</sub> of all four spectra presented in Figure 5(a) is  $4.2 \pm 0.2$  eV, indicating the anhydrous oxide nature of  $\text{La}^{3+}$  cations as observed through NAP-XPS measurements.<sup>40</sup>



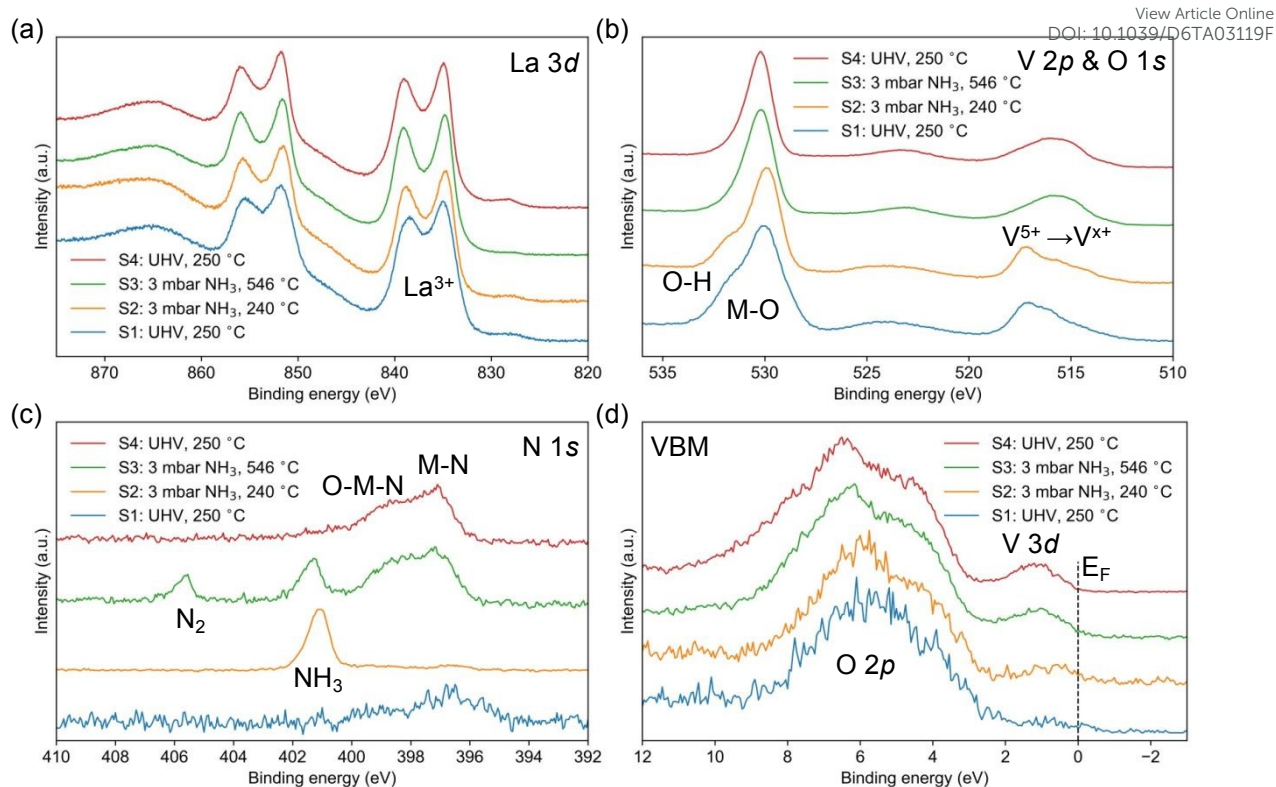


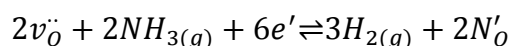
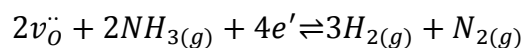
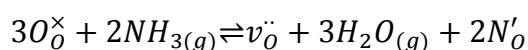
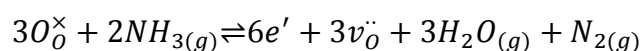
Figure 5 NAP-XPS spectra of (a) La 3d, (b) V 2p and O 1s, (c) N 1s, and (d) VBM in LaVON-S, respectively. The initial number in each legend indicates the measuring sequence. The red circle in (d) indicates the rising valence bands due to the oxynitride formation.

The V cations remained largely stable at 240 °C and were reduced significantly to lower oxidation states at 546 °C, as clearly shown in Figure 5(b). The detailed deconvolution of V  $2p_{3/2}$  is presented in Figure S3 of the supplementary information and Table S2 lists the fitting results of V  $2p_{3/2}$  and O 1s spectra. The atomic ratio of  $V^{5+}$  cations was decreased dramatically from above 40% to below 20%, while that of  $V^{3+}$  cations increased from below 20% to approximately 38%. Zimmerman *et al.* reported satellite peaks in the V 2p spectra of pure vanadium oxides -  $V_2O_5$ ,  $VO_2$  and  $V_2O_3$  - and determined the relative intensities between the corresponding main and satellite peaks.<sup>42,52</sup> The V  $2p_{3/2}$  satellite peaks appear between the V  $2p_{1/2}$  and O 1s signals, while V  $2p_{1/2}$  satellite peaks contribute to the higher binding energy side of the O 1s signals.<sup>42,52</sup> Moreover, V cations in lower oxidation states exhibit stronger satellite peaks due to hybridisation between O 2p orbitals and partially occupied V 3d orbitals - an effect absent for  $V^{5+}$  cations.<sup>42,52</sup> The emergence of such satellite peaks upon reduction of V cations is further confirmed in Figure S4. Meanwhile, the occupation of V 3d states is further evident in the VBM spectra in Figure 5(d), consistent with literature reports.<sup>52</sup> After ammonia evacuation and cooling back to 250 °C, the spectra



remained essentially unchanged, indicating that the reduction of V cations is irreversible under UHV conditions. View Article Online  
DOI: 10.1039/D1TA03119F

The peak-fitted NAP-XPS spectra of the O 1s region are presented in Figure S4. After introducing 3 mbar of ammonia at 546 °C, surface-adsorbed hydroxyl and carbon species were largely dispersed. Notably, the shifts of V 2p<sub>3/2</sub> and O 1s peaks toward higher binding energies are indicative of a Fermi level upshift, likely attributable to the reduction of vanadium cations and the concurrent formation of anion vacancies.<sup>53</sup> This redox process can take place either by exchanging with lattice oxygen or at oxygen vacancy sites expressed as:



Furthermore, the extra formation of the anion vacancy ( $v_{O}^{\bullet}$ ) when exchanging with lattice oxygen is preferred for ammonia decomposition, as suggested by the above computational study.

Prior to exposure to ammonia, the more flattened and noisier nitride signal in the N 1s spectrum recorded at 250 °C under UHV conditions shown in Figure 5(c) compared to that of LaVON-S in Figure 2(d), indicated a lower nitrogen content in LaVON-P, in agreement with the CHN elemental analysis. However, direct quantitative comparison between these two spectra is unreasonable given the different measurement temperatures. Besides, in contrast to LaVON-S, the broad peak in Figure 5(c) also suggests the presence of multiple overlapping nitride/oxynitride species, implying that even the preparation method of parent oxides can influence the subsequent oxynitride formation. The actual composition and O/N ratio are highly sensitive to the temperature, time, and ammonia partial pressure for ammonolysis and any following ammonia annealing process.<sup>45,54</sup> Different local chemical environments such as M-N, N-M-O, M-O-N, and M-N-O have been proposed<sup>55–59</sup>, where “M” denotes the metal cation, while a consensus has not yet been achieved and the localised environment is highly material dependent. Therefore, the peak fitting of nitride/oxynitride species remains extremely difficult and ambiguous. However, the nitride species (M-N) are



always located on the lower binding energy side compared with the oxynitride species due to the larger electronegativity of the O atoms, which reduces the electron density around the N atom.<sup>43,55–58</sup>

When 3 mbar of ammonia was introduced at 240 °C, a distinct N 1s signal emerged, assigned to surface-adsorbed NH<sub>3</sub>, as shown in Figure 5(c) and Figure S5 of the supplementary information. When increasing temperature to 546 °C, strong reduction of V cations and ammonia decomposition promotes the continuous formation of nitride/oxynitride species, alongside the appearance of surface-adsorbed N<sub>2</sub> species.<sup>60</sup> The atomic ratio of O:N shifted from approximately 94.0 %: 6.0 % in the first two steps to about 87.3 %: 12.7 % in the last two steps. The occurrence of ammonia decomposition was further corroborated by residual gas analysis, which showed significantly enhanced signals for N<sub>2</sub> and H<sub>2</sub>, as shown in Figure S6. However, quantitative estimation of the ammonia decomposition rate from mass spectrometry fragments is unreliable for two key reasons: first, the experimental atmosphere (3 mbar NH<sub>3</sub>) does not reflect practical operating conditions for real-world ammonia decomposition applications; second, the gas is largely pumped out before reaching the mass spectrometer due to the differential pumping design of the NAP cell, resulting in a significantly compromised signal-to-noise ratio. Notably, no NO<sub>x</sub> signal was detected in the NAP-XPS spectra, consistent with the absence of NO<sub>x</sub> in the gas phase during catalytic testing, indicating that NO<sub>x</sub> formation is negligible under these conditions. The surface-adsorbed NH<sub>3</sub> and N<sub>2</sub> species were pumped out after ammonia evacuation and cooling back to 250 °C, while the nitride/oxynitride species remained, suggesting that the nitridation is irreversible under UHV conditions.

Apart from the surface-adsorbed species, the broad signals in the binding energy range of 395–402 eV can be deconvoluted into at least three hypothetical peaks contributing nitride/oxynitride species, as summarised in Table S3. As discussed above, the peak with the lowest binding energy can be assigned readily to nitride species, while the other two peaks could represent different oxynitride species. However, it is worth noting that the fitting models presented in Figure S5 and Table S3 represent the best possible fits with the fewest components. The ambiguity is further exacerbated by the low signal intensity and the poor signal-to-noise ratio of the N 1s spectra. Thus, the peak deconvolution of different oxynitride species in the N 1s region



remains controversial, which requires further investigation, particularly with synchrotron and neutron facilities.

View Article Online  
DOI: 10.1039/D6TA03119F

Additionally, the corresponding oxynitride signals are absent in the O 1s spectra, which is likely due to the low concentration of oxynitride species, or absence of oxidised nitrogen with direct O-N bonding in the anion sublattice, and a similar absence has been reported in another study.<sup>59</sup> Moreover, any oxynitride features would overlap with those of hydroxyl groups, making peak fitting even more challenging.

To summarise, the NAP-XAS results clearly exhibit the concurrent reduction of the V cations and the formation of oxynitride species under ammonia conditions at elevated temperatures. Both effects generated additional anion vacancies potentially facilitating the ammonia decomposition reaction.

#### 4. Conclusion

This work demonstrates the potential of  $\text{LaV}(\text{O},\text{N})_{3-\delta}$  perovskite oxynitrides as effective noble metal-free catalysts for ammonia decomposition. The nitrogen content can be readily tuned through different synthesis routes and/or by adjusting the thermal ammonolysis conditions, and the catalytic performance exhibits a strong dependence on the nitrogen content. MLIP simulations further reveal that anion vacancies play a decisive role in promoting ammonia adsorption and decomposition. Complementary NAP-XPS measurements provide direct experimental evidence of dynamic surface processes under operating conditions, capturing continuous surface nitridation during the reaction. Together, these combined experimental and computational insights offer a coherent mechanistic understanding of ammonia decomposition on oxynitrides and highlight the introduction of anion vacancies as a powerful strategy for designing high-performance, noble metal-free catalysts.

#### 5. Author contributions

**Kehan Huang:** Writing – original draft (lead), Writing – review & editing (Equal), Investigation (equal), Formal analysis (lead). **Samia Al Sobhi:** Writing – original draft (equal), Investigation (lead). **Zonghao Shen:** Conceptualization (supporting), Writing – original draft (equal), Writing – review & editing (lead), Project administration. **Zhenzhu Li:** Writing – original draft (supporting), Investigation (Equal). **Alex Walton:**



Investigation (Equal). **Norton West**: Investigation (Equal). **George Wilson**: Investigation (supporting). **Jingdong Xu**: Investigation (supporting). **Stephen J. Skinner**: Conceptualization (lead), Writing – review & editing (Equal), Supervision, Funding acquisition.

## 6. Acknowledgements

This research is funded as part of the project “Decarbonisation with Green Ammonia Using Solid Oxide Fuel Cell for Power Generation (NH<sub>3</sub>-SOFC)” which is part of the CREATE Thematic Programme in Decarbonisation and is supported by the National Research Foundation, Prime Minister’s Office, Singapore under its Campus for Research Excellence and Technological Enterprise (CREATE) programme. SJS thanks the Royal Academy of Engineering for the award of a Research Chair RCSR/2021-1243). This work was supported by the EPSRC National Facility for XPS (“HarwellXPS”, EP/Y023587/1, EP/Y023609/1, EP/Y023536/1, EP/Y023552/1, and EP/Y023544/1) and the Henry Royce Institute for Advanced Materials, funded through EPSRC grants EP/R00661X/1, EP/S019367/1, EP/P025021/1, and EP/P025498/1. We wish to acknowledge the use of the EPSRC funded Physical Sciences Data-science Service hosted by the University of Southampton and STFC under grant number EP/S020357/1.

## 7. Conflict of interest

The authors declare no conflict of interest.

## 8. References

- (1) David, W. I. F.; Agnew, G. D.; Bañares-Alcántara, R.; Barth, J.; Bøgild Hansen, J.; Bréquigny, P.; de Joannon, M.; Fürstenberg Stott, S.; Fürstenberg Stott, C.; Guati-Rojo, A.; Hatzell, M.; MacFarlane, D. R.; Makepeace, J. W.; Mastorakos, E.; Mauss, F.; Medford, A.; Mounaïm-Rousselle, C.; Nowicki, D. A.; Picciani, M. A.; Postma, R. S.; Rouwenhorst, K. H. R.; Sabia, P.; Salmon, N.; Simonov, A. N.; Smith, C.; Torrente-Murciano, L.; Valera-Medina, A. 2023 Roadmap on Ammonia as a Carbon-Free Fuel. *Journal of Physics: Energy* **2024**, *6* (2), 021501. <https://doi.org/10.1088/2515-7655/AD0A3A>.
- (2) Morlanés, N.; Katikaneni, S. P.; Paglieri, S. N.; Harale, A.; Solami, B.; Sarathy, S. M.; Gascon, J. A Technological Roadmap to the Ammonia Energy Economy: Current State and Missing Technologies. *Chemical Engineering Journal* **2021**, *408*, 127310. <https://doi.org/10.1016/J.CEJ.2020.127310>.



- (3) Schüth, F.; Palkovits, R.; Schlögl, R.; Su, D. S. Ammonia as a Possible Element in an Energy Infrastructure: Catalysts for Ammonia Decomposition. *Energy Environ. Sci.* **2012**, *5* (4), 6278–6289. <https://doi.org/10.1039/C2EE02865D>. View Article Online  
DOI: 10.1039/D6TA03119F
- (4) Bell, T. E.; Torrente-Murciano, L. H<sub>2</sub> Production via Ammonia Decomposition Using Non-Noble Metal Catalysts: A Review. *Top. Catal.* **2016**, *59* (15–16), 1438–1457. <https://doi.org/10.1007/S11244-016-0653-4/FIGURES/8>.
- (5) Lamb, K. E.; Dolan, M. D.; Kennedy, D. F. Ammonia for Hydrogen Storage; A Review of Catalytic Ammonia Decomposition and Hydrogen Separation and Purification. *Int. J. Hydrogen Energy* **2019**, *44* (7), 3580–3593. <https://doi.org/10.1016/J.IJHYDENE.2018.12.024>.
- (6) Meng, G.; Jiang, C.; Ma, J.; Ma, Q.; Liu, X. Comparative Study on the Performance of a SDC-Based SOFC Fueled by Ammonia and Hydrogen. *J. Power Sources* **2007**, *173* (1), 189–193. <https://doi.org/10.1016/J.JPOWSOUR.2007.05.002>.
- (7) Rathore, S. S.; Biswas, S.; Fini, D.; Kulkarni, A. P.; Giddey, S. Direct Ammonia Solid-Oxide Fuel Cells: A Review of Progress and Prospects. *Int. J. Hydrogen Energy* **2021**, *46* (71), 35365–35384. <https://doi.org/10.1016/J.IJHYDENE.2021.08.092>.
- (8) Kim, H.; Lee, J. H.; Gokbayrak, A. A.; Seo, Y.; Oh, S.; Oh, M. J.; Jun, Y.; Son, J. W.; Yang, S. Characterization of Direct-Ammonia Solid Oxide Fuel Cells (DA-SOFCs) at 650–750 °C in a Single-Repeating Unit Stack: Effects of Metallic Components and Residual Ammonia. *Int. J. Hydrogen Energy* **2024**, *68*, 1312–1321. <https://doi.org/10.1016/J.IJHYDENE.2024.04.250>.
- (9) Ganley, J. C.; Thomas, F. S.; Seebauer, E. G.; Masel, R. I. A Priori Catalytic Activity Correlations: The Difficult Case of Hydrogen Production from Ammonia. *Catal. Letters* **2004**, *96* (3–4), 117–122. <https://doi.org/10.1023/B:CATL.0000030108.50691.D4>.
- (10) Lucentini, I.; Garcia, X.; Vendrell, X.; Llorca, J. Review of the Decomposition of Ammonia to Generate Hydrogen. *Ind. Eng. Chem. Res.* **2021**, *60* (51), 18560–18611. <https://doi.org/10.1021/ACS.IECR.1C00843>.
- (11) Fang, H.; Liu, D.; Luo, Y.; Zhou, Y.; Liang, S.; Wang, X.; Lin, B.; Jiang, L. Challenges and Opportunities of Ru-Based Catalysts toward the Synthesis and Utilization of Ammonia. *ACS Catal.* **2022**, *12* (7), 3938–3954. <https://doi.org/10.1021/ACSCATAL.2C00090>.
- (12) Sayas, S.; Morlanés, N.; Katikaneni, S. P.; Harale, A.; Solami, B.; Gascon, J. High Pressure Ammonia Decomposition on Ru–K/CaO Catalysts. *Catal. Sci. Technol.* **2020**, *10* (15), 5027–5035. <https://doi.org/10.1039/D0CY00686F>.



- (13) Okura, K.; Okanishi, T.; Muroyama, H.; Matsui, T.; Eguchi, K. Ammonia Decomposition over Nickel Catalysts Supported on Rare-Earth Oxides for the On-Site Generation of Hydrogen. *ChemCatChem* **2016**, *8* (18), 2988–2995. <https://doi.org/10.1002/cctc.201600610>. View Article Online  
DOI: 10.1039/D6TA03119F
- (14) Guo, J.; Wang, P.; Wu, G.; Wu, A.; Hu, D.; Xiong, Z.; Wang, J.; Yu, P.; Chang, F.; Chen, Z.; Chen, P. Lithium Imide Synergy with 3d Transition-Metal Nitrides Leading to Unprecedented Catalytic Activities for Ammonia Decomposition. *Angewandte Chemie* **2015**, *127* (10), 2993–2997. <https://doi.org/10.1002/ange.201410773>.
- (15) Choi, J.-G.; Jung, M.-K.; Choi, S.; Park, T.-K.; Kuk, I. H.; Yoo, J. H.; Park, H. S.; Lee, H.-S.; Ahn, D.-H.; Chung, H. Synthesis and Catalytic Properties of Vanadium Nitrides. *Bull. Chem. Soc. Jpn.* **1997**, *70* (5), 993–996. <https://doi.org/10.1246/bcsj.70.993>.
- (16) Xu, J.; Yan, H.; Jin, Z.; Jia, C. Facile Synthesis of Stable MO<sub>2</sub>N Nanobelts with High Catalytic Activity for Ammonia Decomposition. *Chin. J. Chem.* **2019**, *37* (4), 364–372. <https://doi.org/10.1002/cjoc.201900016>.
- (17) Soerijanto, H.; Rödel, C.; Wild, U.; Lerch, M.; Schomäcker, R.; Schlögl, R.; Ressler, T. The Impact of Nitrogen Mobility on the Activity of Zirconium Oxynitride Catalysts for Ammonia Decomposition. *J. Catal.* **2007**, *250* (1), 19–24. <https://doi.org/10.1016/J.JCAT.2007.04.024>.
- (18) Otremba, T.; Frenzel, N.; Lerch, M.; Ressler, T.; Schomäcker, R. Kinetic Studies on Ammonia Decomposition over Zirconium Oxynitride. *Appl. Catal. A Gen.* **2011**, *392* (1–2), 103–110. <https://doi.org/10.1016/J.APCATA.2010.10.029>.
- (19) Miyashita, K.; Ogasawara, K.; Miyazaki, M.; Abe, H.; Niwa, Y.; Kato, H.; Hosono, H.; Kitano, M. Effects of Nitrogen Vacancy Sites of Oxynitride Support on the Catalytic Activity for Ammonia Decomposition. *NPG Asia Mater.* **2024**, *16* (1), 1–9. <https://doi.org/10.1038/s41427-024-00572-6>.
- (20) Fuertes, A. Chemistry and Applications of Oxynitride Perovskites. *J. Mater. Chem.* **2012**, *22* (8), 3293–3299. <https://doi.org/10.1039/C2JM13182J>.
- (21) Kageyama, H.; Hayashi, K.; Maeda, K.; Attfield, J. P.; Hiroi, Z.; Rondinelli, J. M.; Poeppelmeier, K. R. Expanding Frontiers in Materials Chemistry and Physics with Multiple Anions. *Nat. Commun.* **2018**, *9* (1), 772-. <https://doi.org/10.1038/S41467-018-02838-4>.
- (22) Harada, J. K.; Charles, N.; Poeppelmeier, K. R.; Rondinelli, J. M. Heteroanionic Materials by Design: Progress Toward Targeted Properties. *Advanced Materials* **2019**, *31* (19), 1805295. <https://doi.org/10.1002/ADMA.201805295>.



- (23) Kim, Y. Il; Woodward, P. M.; Baba-Kishi, K. Z.; Tai, C. W. Characterization of the Structural, Optical, and Dielectric Properties of Oxynitride Perovskites AMO<sub>2</sub>N (A = Ba, Sr, Ca; M = Ta, Nb). *Chemistry of Materials* **2004**, *16* (7), 1267–1276. <https://doi.org/10.1021/CM034756J>. View Article Online  
DOI: 10.1039/D6TA03119F
- (24) Logvinovich, D.; Ebbinghaus, S. G.; Reller, A.; Marozau, I.; Ferri, D.; Weidenkaff, A. Synthesis, Crystal Structure and Optical Properties of LaNbON<sub>2</sub>. *Z. Anorg. Allg. Chem.* **2010**, *636* (6), 905–912. <https://doi.org/10.1002/ZAAC.201000067>.
- (25) Shen, Z.; Wu, J.; Shorvon, M. W.; Cazaux, G.; Parker, S. C.; Skinner, S. J. Partially Anion-Ordered Cerium Niobium Oxynitride Perovskite Phase with a Small Band Gap. *Chemistry of Materials* **2021**, *33* (11), 4045–4056. <https://doi.org/10.1021/ACS.CHEMMATER.1C00631>.
- (26) Atfield, J. P. Principles and Applications of Anion Order in Solid Oxynitrides. *Cryst. Growth Des.* **2013**, *13* (10), 4623–4629. <https://doi.org/10.1021/CG4011168>.
- (27) Yang, M.; Oró-Solée, J.; Rodgers, J. A.; Jorge, A. B.; Fuertes, A.; Atfield, J. P. Anion Order in Perovskite Oxynitrides. *Nat. Chem.* **2010**, *3* (1), 47–52. <https://doi.org/10.1038/nchem.908>.
- (28) Clarke, S. J.; Hardstone, K. A.; Michie, C. W.; Rosseinsky, M. J. High-Temperature Synthesis and Structures of Perovskite and n = 1 Ruddlesden–Popper Tantalum Oxynitrides. *Chemistry of Materials* **2002**, *14* (6), 2664–2669. <https://doi.org/10.1021/CM011738Y>.
- (29) Ebbinghaus, S. G.; Weidenkaff, A.; Rachel, A.; Reller, A. Powder Neutron Diffraction of SrNbO<sub>2</sub>N at Room Temperature and 1.5 K. *Acta Crystallogr. C* **2004**, *60* (9), i91–i93. <https://doi.org/10.1107/S0108270104016105>.
- (30) Logvinovich, D.; Bocher, L.; Sheptyakov, D.; Figi, R.; Ebbinghaus, S. G.; Aguiar, R.; Aguirre, M. H.; Reller, A.; Weidenkaff, A. Microstructure, Surface Composition and Chemical Stability of Partly Ordered LaTiO<sub>2</sub>N. *Solid State Sci.* **2009**, *11* (8), 1513–1519. <https://doi.org/10.1016/J.SOLIDSTATESCIENCES.2009.05.024>.
- (31) Seo, J.; Hisatomi, T.; Nakabayashi, M.; Shibata, N.; Minegishi, T.; Katayama, M.; Domen, K. Efficient Solar-Driven Water Oxidation over Perovskite-Type BaNbO<sub>2</sub>N Photoanodes Absorbing Visible Light up to 740 Nm. *Adv. Energy Mater.* **2018**, *8* (24), 1800094. <https://doi.org/10.1002/AENM.201800094>.
- (32) Aguiar, R.; Kalytta, A.; Reller, A.; Weidenkaff, A.; Ebbinghaus, S. G. Photocatalytic Decomposition of Acetone Using LaTi(O,N)<sub>3</sub> Nanoparticles under Visible Light Irradiation. *J. Mater. Chem.* **2008**, *18* (36), 4260–4265. <https://doi.org/10.1039/B806794E>.



- (33) Sun, X.; Mi, Y.; Jiao, F.; Xu, X. Activating Layered Perovskite Compound Sr<sub>2</sub>TiO<sub>4</sub> via La/N Codoping for Visible Light Photocatalytic Water Splitting. *ACS Catal.* **2018**, *8* (4), 3209–3221. <https://doi.org/10.1021/ACSCATAL.8B00369>. View Article Online  
DOI: 10.1039/D6TA03119F
- (34) Yoon, S.; Maegli, A. E.; Karvonen, L.; Shkabko, A.; Populoh, S.; Gałazka, K.; Sagarna, L.; Aguirre, M. H.; Jakes, P.; Eichel, R. A.; Ebbinghaus, S. G.; Pokrant, S.; Weidenkaff, A. Synthesis, Crystal Structure, Electric and Magnetic Properties of LaVO<sub>2.78</sub>N<sub>0.10</sub>. *Z. Anorg. Allg. Chem.* **2014**, *640* (5), 797–804. <https://doi.org/10.1002/ZAAC.201300593>.
- (35) Toby, B. H.; Von Dreele, R. B. GSAS-II: The Genesis of a Modern Open-Source All Purpose Crystallography Software Package. *J. Appl. Crystallogr.* **2013**, *46* (2), 544–549. <https://doi.org/10.1107/S0021889813003531>.
- (36) Batatia, I.; Lin, C.; Hart, J.; Kasoar, E.; Elena, A. M.; Norwood, S. W.; Wolf, T.; Csányi, G. Cross Learning between Electronic Structure Theories for Unifying Molecular, Surface, and Inorganic Crystal Foundation Force Fields. *arXiv preprint* **2025**. <https://doi.org/10.48550/arXiv.2510.25380>.
- (37) Batatia, I.; Kovács, D. P.; Simm, G. N. C.; Ortner, C.; Csányi, G. MACE: Higher Order Equivariant Message Passing Neural Networks for Fast and Accurate Force Fields. In *Advances in Neural Information Processing Systems*; 2022; Vol. 35, pp 11423–11436.
- (38) Larsen, A. H.; Mortensen, J. J.; Blomqvist, J.; Castelli, I. E.; Christensen, R.; Dułak, M.; Friis, J.; Groves, M. N.; Hammer, B.; Hargus, C.; Hermes, E. D.; Jennings, P. C.; Jensen, P. B.; Kermode, J.; Kitchin, J. R.; Kolsbjerg, E. L.; Kubal, J.; Kaasbjerg, K.; Lysgaard, S.; Maronsson, J. B.; Maxson, T.; Olsen, T.; Pastewka, L.; Peterson, A.; Rostgaard, C.; Schiøtz, J.; Schütt, O.; Strange, M.; Thygesen, K. S.; Vegge, T.; Vilhelmsen, L.; Walter, M.; Zeng, Z.; Jacobsen, K. W. The Atomic Simulation Environment—a Python Library for Working with Atoms. *Journal of Physics: Condensed Matter* **2017**, *29* (27), 273002. <https://doi.org/10.1088/1361-648X/AA680E>.
- (39) Bahn, S. R.; Jacobsen, K. W. An Object-Oriented Scripting Interface to a Legacy Electronic Structure Code. *Comput. Sci. Eng.* **2002**, *4* (3), 56–66. <https://doi.org/10.1109/5992.998641>.
- (40) Sunding, M. F.; Hadidi, K.; Diplas, S.; Løvvik, O. M.; Norby, T. E.; Gunnæs, A. E. XPS Characterisation of in Situ Treated Lanthanum Oxide and Hydroxide Using Tailored Charge Referencing and Peak Fitting Procedures. *J. Electron Spectros. Relat. Phenomena* **2011**, *184* (7), 399–409. <https://doi.org/10.1016/J.ELSPEC.2011.04.002>.
- (41) Biesinger, M. C.; Lau, L. W. M.; Gerson, A. R.; Smart, R. S. C. Resolving Surface Chemical States in XPS Analysis of First Row Transition Metals,



Oxides and Hydroxides: Sc, Ti, V, Cu and Zn. *Appl. Surf. Sci.* **2010**, *257* (3), 887–898. <https://doi.org/10.1016/J.APSUSC.2010.07.086>. View Article Online  
DOI: 10.1039/D6TA03119F

- (42) Silversmit, G.; Depla, D.; Poelman, H.; Marin, G. B.; De Gryse, R. Determination of the V2p XPS Binding Energies for Different Vanadium Oxidation States (V5+ to V0+). *J. Electron Spectros. Relat. Phenomena* **2004**, *135* (2–3), 167–175. <https://doi.org/10.1016/J.ELSPEC.2004.03.004>.
- (43) Balogun, K.; Ganesan, A.; Chukwunenye, P.; Gharaee, M.; Adesope, Q.; Nemšák, S.; Bagus, P. S.; Cundari, T. R.; D'Souza, F.; Kelber, J. A. Vanadium Oxide, Vanadium Oxynitride, and Cobalt Oxynitride as Electrocatalysts for the Nitrogen Reduction Reaction: A Review of Recent Developments. *Journal of Physics: Condensed Matter* **2023**, *35* (33), 333002. <https://doi.org/10.1088/1361-648X/ACD49D>.
- (44) Masuda, Y.; Mashima, R.; Yamada, M.; Ikeuchi, K.; Murai, K. I.; Waterhouse, G. I. N.; Metson, J. B.; Moriga, T. Relationship between Anion and Cation Nonstoichiometries and Valence State of Titanium in Perovskite-Type Oxynitrides LaTiO2N. *Journal of the Ceramic Society of Japan* **2009**, *117* (1361), 76–81. <https://doi.org/10.2109/JCERSJ.117.76>.
- (45) Clarke, S. J.; Guinot, B. P.; Michie, C. W.; Calmont, M. J. C.; Rosseinsky, M. J. Oxynitride Perovskites: Synthesis and Structures of LaZrO2N, NdTiO2N, and LaTiO2N and Comparison with Oxide Perovskites. *Chemistry of Materials* **2001**, *14* (1), 288–294. <https://doi.org/10.1021/CM010577V>.
- (46) Clark, L.; Oró-Solé, J.; Knight, K. S.; Fuertes, A.; Atfield, J. P. Thermally Robust Anion-Chain Order in Oxynitride Perovskites. *Chemistry of Materials* **2013**, *25* (24), 5004–5011. <https://doi.org/10.1021/CM4037132>.
- (47) Jolaoso, L. A.; Zaman, S. F.; Podila, S.; Driss, H.; Al-Zahrani, A. A.; Daous, M. A.; Petrov, L. Ammonia Decomposition over Citric Acid Induced  $\gamma$ -Mo2N and Co3Mo3N Catalysts. *Int. J. Hydrogen Energy* **2018**, *43* (10), 4839–4844. <https://doi.org/10.1016/J.IJHYDENE.2018.01.092>.
- (48) Bell, T. E.; Ménard, H.; González Carballo, J. M.; Tooze, R.; Torrente-Murciano, L. Hydrogen Production from Ammonia Decomposition Using Co/ $\gamma$ -Al2O3 Catalysts – Insights into the Effect of Synthetic Method. *Int. J. Hydrogen Energy* **2020**, *45* (51), 27210–27220. <https://doi.org/10.1016/J.IJHYDENE.2020.07.090>.
- (49) Srifa, A.; Okura, K.; Okanishi, T.; Muroyama, H.; Matsui, T.; Eguchi, K. COx-Free Hydrogen Production via Ammonia Decomposition over Molybdenum Nitride-Based Catalysts. *Catal. Sci. Technol.* **2016**, *6* (20), 7495–7504. <https://doi.org/10.1039/C6CY01566B>.



- (50) Soerijanto, H. Catalytic On-Board Hydrogen Production from Methanol and Ammonia for Mobile Application. Thesis or dissertation, Technische Universität Berlin, 2007. <https://doi.org/10.14279/DEPOSITONCE-1757>. View Article Online  
DOI: 10.1039/D6TA03119F
- (51) Chellappa, A. S.; Fischer, C. M.; Thomson, W. J. Ammonia Decomposition Kinetics over Ni-Pt/Al<sub>2</sub>O<sub>3</sub> for PEM Fuel Cell Applications. *Appl. Catal. A Gen.* **2002**, 227 (1–2), 231–240. [https://doi.org/10.1016/S0926-860X\(01\)00941-3](https://doi.org/10.1016/S0926-860X(01)00941-3).
- (52) Zimmermann, R.; Claessen, R.; Reinert, F.; Steiner, P.; Hüfner, S. Strong Hybridization in Vanadium Oxides: Evidence from Photoemission and Absorption Spectroscopy. *Journal of Physics: Condensed Matter* **1998**, 10 (25), 5697. <https://doi.org/10.1088/0953-8984/10/25/018>.
- (53) Wang, J.; Mueller, D. N.; Crumlin, E. J. Recommended Strategies for Quantifying Oxygen Vacancies with X-Ray Photoelectron Spectroscopy. *J. Eur. Ceram. Soc.* **2024**, 44 (15), 116709. <https://doi.org/10.1016/J.JEURCERAMSOC.2024.116709>.
- (54) Kim, Y. II. Effects of KCl Flux on the Morphology, Anion Composition, and Chromaticity of Perovskite Oxynitrides, CaTaO<sub>2</sub>N, SrTaO<sub>2</sub>N, and LaTaO<sub>2</sub>N. *Ceram. Int.* **2014**, 40 (4), 5275–5281. <https://doi.org/10.1016/J.CERAMINT.2013.10.100>.
- (55) Wang, D. H.; Jia, L.; Wu, X. L.; Lu, L. Q.; Xu, A. W. One-Step Hydrothermal Synthesis of N-Doped TiO<sub>2</sub>/C Nanocomposites with High Visible Light Photocatalytic Activity. *Nanoscale* **2012**, 4 (2), 576–584. <https://doi.org/10.1039/C1NR11353D>.
- (56) Xing, M.; Zhang, J.; Chen, F. New Approaches to Prepare Nitrogen-Doped TiO<sub>2</sub> Photocatalysts and Study on Their Photocatalytic Activities in Visible Light. *Appl. Catal. B* **2009**, 89 (3–4), 563–569. <https://doi.org/10.1016/J.APCATB.2009.01.016>.
- (57) Etacheri, V.; Seery, M. K.; Hinder, S. J.; Pillai, S. C. Highly Visible Light Active TiO<sub>2</sub>-xNx Heterojunction Photocatalysts. *Chemistry of Materials* **2010**, 22 (13), 3843–3853. <https://doi.org/10.1021/CM903260F>.
- (58) Zou, F.; Jiang, Z.; Qin, X.; Zhao, Y.; Jiang, L.; Zhi, J.; Xiao, T.; Edwards, P. P. Template-Free Synthesis of Mesoporous N-Doped SrTiO<sub>3</sub> Perovskite with High Visible-Light-Driven Photocatalytic Activity. *Chemical Communications* **2012**, 48 (68), 8514–8516. <https://doi.org/10.1039/C2CC33797E>.
- (59) Mi, Y. Y.; Yu, Z.; Wang, S. J.; Gao, X. Y.; Wee, A. T. S.; Ong, C. K.; Huan, C. H. A. Thermal Stability of Nitrogen-Doped SrTiO<sub>3</sub> Films: Electronic and Optical Properties Studies. *J. Appl. Phys.* **2007**, 101 (6), 63708. <https://doi.org/10.1063/1.2713350/1028237>.



- (60) Zahra, K. M.; Byrne, C.; Alieva, A.; Casiraghi, C.; Walton, A. S. Intercalation, Decomposition, Entrapment – a New Route to Graphene Nanobubbles. *Physical Chemistry Chemical Physics* **2020**, 22 (14), 7606–7615. <https://doi.org/10.1039/d0cp00592d>. [View Article Online](#)  
DOI: 10.1039/D6TA03119F



### Data Availability Statement

View Article Online  
DOI: 10.1039/D6TA03119F

The research data that supports this article are available on Zenodo  
(<https://zenodo.org/communities/electroceramic-materials>)

